JOURNAL OF SPACECRAFT AND ROCKETS
Vol. 41, No. 4, July–August 2004

# Active Plasma Experiment: North Star Particle Data

K. A. Lynch*
*Dartmouth College, Hanover, New Hampshire 03755*
R. B. Torbert† and M. Chutter‡
*University of New Hampshire, Durham, New Hampshire 03824*
R. E. Erlandson§ and C. I. Meng¶
*Johns Hopkins University, Applied Physics Laboratory, Laurel, Maryland 20723-6099*
and
J. I. Zetzer,**B. G. Gavrilov,†† and Y. Kiselev‡‡
*Russian Academy of Sciences, 117334, Moscow, Russia*

**We report on data from particle instruments making in situ sounding rocket measurements of the particle environment within and near an aluminum plasma jet caused by an explosion in the auroral ionosphere. The Active Plasma Experiment sounding rocket was launched to an altitude of 350 km from the Poker Flat Research Range in January 1999. The payload separated after launch into observing payloads and two explosive plasma jet generators. During the flight, the two explosive packages were detonated, and the observing payloads studied the surrounding environment. The particle instruments measured the resulting plasma jet from a distance of approximately 500 m. The instruments measured ions from 10 to 420 eV, electrons from 10 to 6000 eV, and low-energy electrons from 2 to 1200 eV. After each explosion, the particle instruments recorded the passage of a burst of material past the spacecraft. Analysis of mass-dependent effects, plasma $\beta$, and critical ionization velocity parameters are presented, together with a comparison to earlier experimental observations. In particular we note that the duration of the enhanced ion fluxes is controlled by the jet velocity and drops sharply when the jet velocity falls below the critical ionization velocity for each ion, with the peak ion fluxes only observed while $v_{\text{jet}} > V_{\text{crit}}(\text{O+})$.**

## Nomenclature

| | | |
|---|---|---|
| $B$ | = | magnetic field strength |
| $e$ | = | electronic charge |
| $f$ | = | distribution function |
| $k_B$ | = | Boltzmann constant |
| $m$ | = | atomic mass of neutral gas |
| $m_i$ | = | ion mass |
| $n_e$ | = | electron number density |
| $n_e v_e$ | = | heated electron flux |
| $n_i$ | = | ion number density |
| $n_n$ | = | neutral density |
| $T_e$ | = | electron temperature |
| $V_{\text{crit}}$ | = | critical ionization velocity |
| $v_{\text{jet}}$ | = | velocity of jet |
| $\beta$ | = | plasma beta; ratio of magnetic to kinetic pressure |
| $\epsilon_e$ | = | electron energy |
| $\epsilon_i$ | = | ion energy |
| $\eta$ | = | efficiency factor |
| $\mu_0$ | = | permeability of free space |
| $\sigma$ | = | collisional cross section of aluminum |
| $\Phi$ | = | ionization potential of atoms in neutral gas |

Received 19 October 2001; revision received 18 November 2002; accepted for publication 30 August 2003. 

*Assistant Professor of Physics and Astronomy, Department of Physics and Astronomy, Wilder Laboratory 6127.
†Professor of Physics, Institute for the Study of Earth Oceans and Space.
‡Computer Specialist, Institute for the Study of Earth Oceans and Space.
§Assistant Group Supervisor, Space Department, 11100 Johns Hopkins Road. Member AIAA.
¶Branch Supervisor, Space Department, 11100 Johns Hopkins Road. Member AIAA.
**Deputy Director, Institute of Geospheres Dynamics.
††Head of Laboratory, Institute of Geospheres Dynamics.
‡‡Senior Scientist, Institute of Geospheres Dynamics.

## Introduction

THE Active Plasma Experiment (APEX) mission was a sounding-rocket-based active experiment in the auroral ionosphere.[1,2] The plasma effects of explosions from two aluminum explosive packages (explosive-type generators, or ETG1 and ETG2) were observed from three separate payload observation points [plasma diagnostic payload (PDP) and optical sensor payload; the ETG1 event was also monitored by instrumentation on the ETG2 payload]. To accomplish this, the single launch payload was separated inflight into an array of four separate pieces. The experiment was conducted in the premidnight auroral ionosphere, at approximately 350 km altitude. The plasma jets from the explosive packages were released in a direction nearly perpendicular to the Earth's magnetic field, carrying high-speed plasma, neutral particles, and a strong diamagnetic cavity past the three observational packages in the array of payloads. The APEX instrumentation was designed to study the interactions between the jet and the environment (both plasma and neutral) and to study the long-duration interactions between the plasma cloud and the environment. Several other papers in this issue[2–4] describe various aspects of this experiment.

Other sounding-rocket studies, with barium or strontium rather than aluminum releases, have examined critical-ionization-velocity (CIV) effects[5–7] of a plasma jet ejected at an angle oblique to $\boldsymbol{B}$. CIV effects occur when a plasma and a neutral gas stream with respect to each other at a high enough velocity that the neutral gas becomes ionized through collisions with the plasma. These effects were predicted theoretically some time ago,[5] but have been notoriously difficult to measure in space. The critical velocity for ionization, perpendicular to the local magnetic field, is given by

$$V_{\text{crit}} = \sqrt{2e\Phi/m} \tag{1}$$

For relative streaming speeds greater than $V_{\text{crit}}$, Alfvén conjectured that the neutral gas becomes ionized. The resulting ion beam is thought to excite a linear ion beam instability, which will heat the plasma electrons sufficiently to then create even more ions.[8]

This feedback mechanism can result in rapid ionization, and one barium-shaped-charged release experiment (Project Porcupine)

showed that yields (ratio of ions produced to neutral jet density) of over 10% are possible.[6] Other experiments (CONDOR)[9] have had unexplainably small yields, despite observations of sufficient levels of lower hybrid wave activity needed to activate the expected feedback mechanism. In the CRIT II study[10–13] in addition to the expected ionization of the barium neutrals from the release experiment, ambient ionospheric oxygen was also ionized.

The observational goal of the APEX particle detectors was measurement of the plasma particle effects caused by the explosions. Specifically, the detectors were designed to quantify and time the electron density and temperature caused by the explosions, over a large range of energy and flux, and quantify and time the ion flux resulting from the explosions, in particular looking for critical ionization velocity effects.

In this paper we present these data, in particular noting mass-dependent effects in the ion data. We compare our particle flux measurements to those of the onboard Langmuir-probe measurements[3] and to the onboard magnetometer and very low-frequency (VLF) electric field data.[4] We examine electron heating and calculate a plasma $\beta$ using the electron data. We present an analysis of the observed CIV effects and compare to the earlier CRIT II study.

## Particle Instrument Descriptions

The instruments that are the focus of this paper were mounted on the payload-diagnostic-package (PDP) payload of the APEX mission. All three sensors were top-hat-style hemispherical electrostatic analyzers (ESAs), an energy- and pitch-angle-imaging instrument in common use in auroral particle measurements.[14] These detectors have a 2-$\pi$ planar field of view. They are calibrated preflight using a variable energy electron or ion gun in a vacuum chamber. The sensor element is a pair of microchannel plates. To avoid high-voltage arcing, no high voltage is applied to the detector until the payload has passed above the atmosphere in its trajectory.

Figure 1 shows the instruments mounted on the PDP payload. In this figure, the jet impinges nominally from the right, and the magnetic field direction is nominally downward. The medium-electron ESA (MESA) is the electron detector mounted opposite the ion electrostatic analyser (IESA); the small-electron ESA (SESA) is the electron detector mounted with a magnetometer on a spin-axis aligned boom. Table 1 lists various parameters of the three top-hat analyzers, including the pitch angle and energy resolution for each.

The geometry factor needed for the IESA was somewhat smaller than that for the equivalent CRIT II experiment detector because the shorter distance between the explosion and the observation for APEX meant that a larger particle flux was expected. The IESA was mounted on the PDP such that its aperture plane was parallel to the PDP spin axis. (In the left panel of Fig. 1, this aperture plane includes the horizontal axis and the normal to the page.) This mounting arrangement was chosen so that for nominal PDP attitude channel 8 of the IESA would always look in the expected direction of incoming jet, independent of the PDP spin phase. The angular acceptance width of the aperture normal to the aperture plane was ±2.5 deg. Although the IESA is not a mass-analyzing instrument,

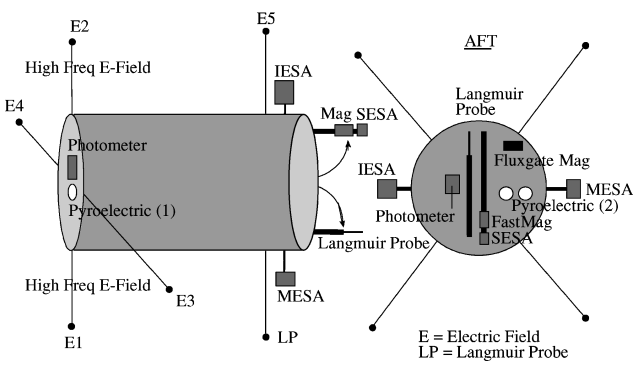


**Fig. 1 APEX particle instruments mounted on the PDP payload.**

**Table 1 Particle detector instrumentation**

| Parameter | IESA | MESA | SESA |
|---|---|---|---|
| $G_0$ per bin, cm$^2$ sr s (keV/keV) | 1.38$e$−5 | 5$e$−4 | 3$e$−5 |
| Bin size, deg | 17 | 17 | 34 |
| No. bins | 15 | 15 | 7 |
| No. energy steps | 15 | 15 | 15 |
| Energy step, ms | 0.4 | 0.4 | 0.4 |
| Sweep time, ms | 6.4 | 6.4 | 6.4 |
| Energy range, eV | 10–420 | 10–10,000 | 2–2,000 |
| Energy resolution, % | 15 | 15 | 7 |
| Angular resolution, deg | 17 | 17 | 34 |

time-of-flight delays from the explosion to the detector can provide mass information in this case.

The MESA had a large geometry factor. The MESA was mounted on the PDP in the a manner symmetric to the IESA, so that again its channel 8 was always looking toward the incoming jet independent of the PDP spin phase. The 15 pitch-angle bins were set preflight to variable in-plane widths to control the expected dynamic range; the jet-looking bin was stopped down mechanically to 17% of full width.

The SESA had a smaller geometry factor and a lower energy range. Because the main purpose of the SESA was to look for low-energy-field-aligned electrons excited by the explosion, the SESA was mounted on the PDP such that its aperture plane was perpendicular to the PDP spin axis; in this way, one channel was always field aligned if the spin axis remained perpendicular to $\boldsymbol{B}$. In Fig. 1, this detector is shown mounted together with a magnetometer on a spin-axis-aligned boom. Its aperture plane is normal to the boom direction.

We will show in this paper that other data come from some of the onboard Langmuir probes. There are two on the PDP: a thin probe that saturates at densities of $10^8$/cc and a thick probe that can measure up to $10^{11}$/cc. Also we show data from the "thick" probe on the ETG2 payload. These Langmuir probes have higher time resolution and are sensitive to lower-energy particles than the particle instrumentation just described. The Langmuir probes work in a fixed-bias mode ($V_p = -10$ V) and collect ion saturation current.

## Data Summary: Cavity Passage and Particle Speeds

After each of the explosive events, the disturbance from the explosion propagates outward, moving across the diagnostic payload array. The signatures of the disturbance include a sharp increase in plasma density (a density enhancement) and an accompanying decrease in magnetic field strength (a diamagnetic cavity); the disturbance is generally referred to as a cavity, referring to the diamagnetic effect. The high-temperature and density plasma in the density enhancement repels the local geomagnetic field, pushing the field lines away from the cavity. We can observe this disturbance in many ways, including the Langmuir-probe density data and the magnetometer dc field data. Figure 2 shows the cavity passage from the first explosion (ETG1) as seen by the onboard Langmuir-probe instrumentation.[3] The enhancement is seen first on the nearby ETG2 payload (red trace, rising at $T + 0.004$ s) and next on the PDP (green and orange traces, rising at $T + 0.014$ s). These data are shown as a function of time since the first explosion at $T_{\text{etg1}} = 345.137$. The Langmuir probes show the passage of the plasma enhancement; the strong diamagnetic cavity (not shown here) is coincident, with the sharpest gradients in the field strength seen at the times of the peaks in density on the PDP at $T_{\text{etg1}} + 0.0175$ and just before $T_{\text{etg1}} + 0.03$. At the PDP location, the cavity/enhancement was 300 m across and traveling at 25–30 km/s perpendicular to $\boldsymbol{B}$; it was observed on the PDP from $T + 345.155$ to $T + 345.167$, or from $T_{\text{etg1}} + 0.0175$ to just before 0.03 s after the explosion at $T_{\text{etg1}} = 345.137$. Timing information throughout this paper is known to better than 1 ms.

The two PDP traces shown in Fig. 2 reflect the different sensitivity of the two Langmuir probes. The lower sensitivity instrument has

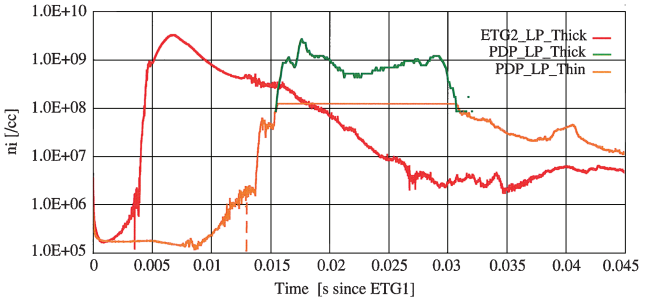


**Fig. 2 Cavity passage as seen by the IDG Langmuir probes, two on the PDP payload and one on the ETG2 payload. The resolution of these Langmuir probes is $\pm 10^4$/cc.**

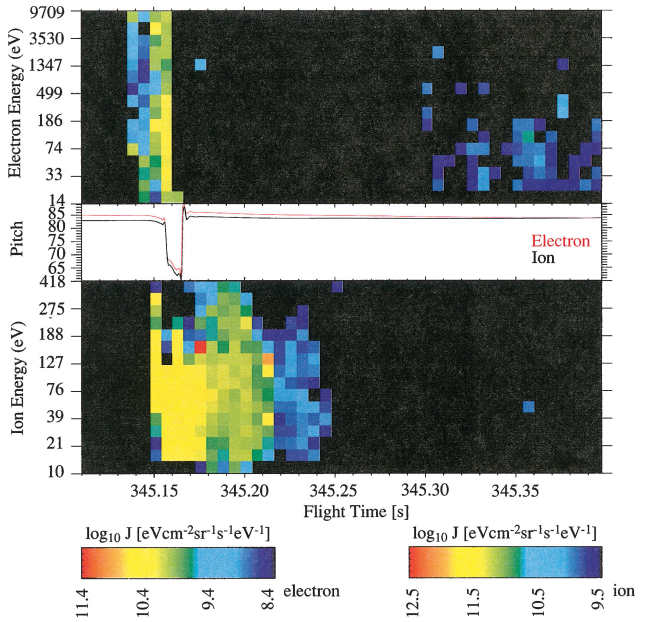


**Fig. 3 Electron and ion energy vs time in the jet direction, for the top and bottom panels, respectively, from the MESA and IESA detectors. Energy and pitch-angle resolution for these detectors are given in Table 1. Error in the flux, as described in text, is given by $\sqrt{(J_E/G_0)}$, where $G_0$ is given in Table 1. For the middle panel, pitch angle of jet-looking particle detector bins, calculated from onboard magnetometer data as a function of time. The diamagnetic cavity disrupts this calculation, and the abrupt changes in "pitch" mark the edges of the cavity.**

a response similar to that of the particle instrumentation described here. Note the early arrival of a small flux of high-velocity ions before the diamagnetic cavity onset at $T_{etg1} = 0.0175$. This low-flux, high-speed precursor will be seen also in the leading edge of the event as seen by the IESA detector next.

The particle instruments complement the Langmuir-probe data by providing energy spectra and pitch-angle information. The succeeding figures show these data. For all of these succeeding figures, resolution and error calculations are as follows. Energy and pitch-angle resolution for each detector are listed in Table 1. Error in the flux is given by Poisson statistics of the counting rates. Because the flux is given by the counts divided by the geometry factor $J_E = C/G_0$, the error in the flux can be calculated as $\delta J_E = \sqrt{C}/G_0 = \sqrt{(J_E * G_0)}/G_0 = \sqrt{(J_E/G_0)}$. The geometry factor $G_0$ is also given in Table 1 for each detector.

Figure 3 shows electron and ion differential fluxes from the MESA and IESA as functions of energy vs time, from the directional bin looking towards the oncoming jet (bin 8). The electron data are saturated from $T + 345.165$ s until approximately $T + 345.3$ s.

The center panels of Figs. 3–5 show the pitch angle of particles accepted by the jet-looking bins, as calculated from the onboard magnetometer data. This parameter provides an excellent qualitative indication of the passage of the diamagnetic cavity, as the background magnetic field (and therefore the pitch angle calculated for a given bin at a given time) deviates significantly within the diamagnetic cavity. Thus the abrupt changes in the calculated pitch angle demarcate the edges of the cavity as it passes the PDP.

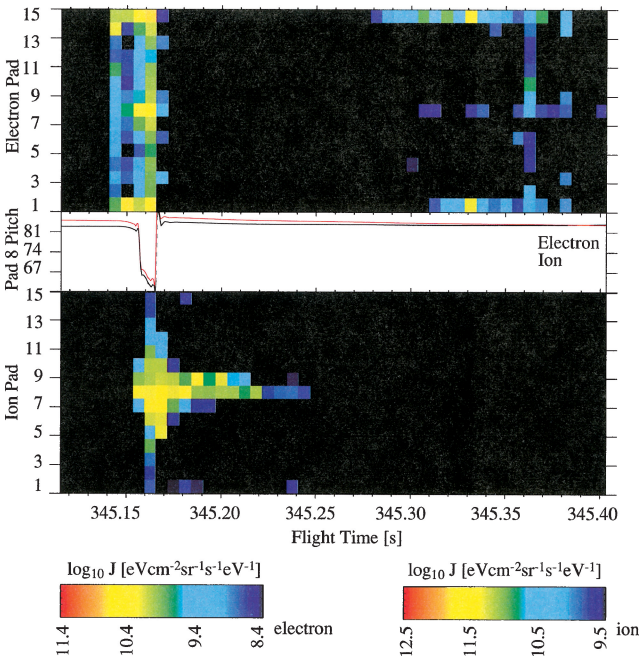


**Fig. 4 Electron and ion look angle vs time summed over all energies, from the MESA and IESA detectors. The cental bin (pad 8) looks into the jet. The opposing bins (pads 1, 15) look antiparallel to the jet. Resolution and errors as in Fig. 3. The middle panel shows pitch-angle information as in Fig. 3; the deviation marks the diamagnetic cavity.**

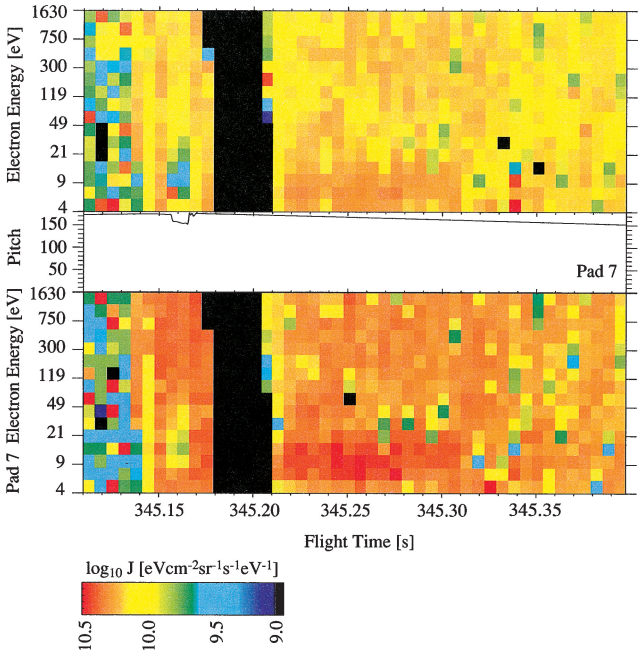


**Fig. 5 Low-energy electron energy spectra data, from the SESA detector. Resolution and errors as in Fig. 3. The middle panel shows pitch-angle information as in Fig. 3; the deviation marks the diamagnetic cavity.**

Figure 4 shows electron and ion differential fluxes as functions of detector look angle vs time, summed over all energies. Note the fluxes of both ions and electrons antiparallel to the jet, in bins 1 and 15. Figure 5 shows low-energy electron energy spectra from the SESA instrument, summed over all look directions (top) and focusing on the most-field-aligned direction (bottom). Note that the

SESA also saturates (from $T + 345.178$ to $T + 345.215$) but for a shorter and later time than the MESA.

For the first explosion (the data shown here), the ion burst (Figs. 3 and 4, lower panels) was coincident with the diamagnetic cavity recorded by the magnetometers (Figs. 3 and 4, center panels). The electron burst (Figs. 3 and 4, top panels) was also most intense at this time (indeed saturating the detectors from $T + 345.16$ to $T + 345.3$) but was observable for a longer time, being measurable (after the saturation) for nearly half a second. The particles in these detectors (energies above 10 eV) were seen predominantly in the direction of the jet (Fig. 4, ion and electron pads 8). However, the lowest-energy electrons (lower energy range of Fig. 5) showed a preference for the field-aligned direction (pad 7, perpendicular to the jet). There are also indications of some particles, both electrons and ions, moving opposite to the jet velocity (Fig. 4, pads 1 and 15). For the second explosion (not shown), where the payloads' separation vector was not as well aligned with the jet, the detectors also observed the jet but did not saturate.

In the particle data for the first event, the high-speed particles reach the diagnostics payload just before the diamagnetic cavity, matching the Institute of Geospheres Dynamics Langmuir probe result. Compare, in Fig. 3, the onset of the ion data enhancement and the abrupt change in "pitch." This precursor is also seen in the Langmuir-probe data, as noted in the discussion of Fig. 2. The highest-speed ions travel the $466 \pm 5$ m distance in 0.013 s, a speed of almost $36 \pm 3$ km/s. With the particle detector data, we can examine the mass-dependent time-of-flight effects, measure the plasma heating and plasma pressure in the diamagnetic cavity, and study critical ionization velocity effects in the resulting ion cloud, as described next.

## Mass Analysis and Particle Motions

Given a PDP-ETG1 payload separation distance of $466 \pm 5$ m and a first explosion time $T_{\text{etg1}}$ of $T + 345.137$ s, we can use time-of-flight measurements to interpret the complex energy spectrum of the ions hitting the diagnostic package as composed of different masses all traveling at the jet speed. Neutral oxygen, aluminum, and other gasses traveling at the jet speed and being ionized near the PDP will appear in the IESA as energetic ions with energy

$$\epsilon_i = 0.5 * m_i * v_{\text{jet}}^2 \tag{2}$$

where $v_{\text{jet}}$ can be calculated as $466 \text{ m}/(T - T_{\text{etg1}})$. Figure 6 shows the onset of count rate in the particle detectors as a function of time from $T_{\text{etg1}}$. The prompt response in the electron detectors, before the onset of the cavity at $T_{\text{etg1}} + 0.0175$ s, is a response to UV. Figure 7 shows the ion mass spectrum inferred from the assumption that the different energies observed in the first sweep of the ion detector (Fig. 6a; from $T_{\text{etg1}} = 0.0125$ to 0.0175 s) come from different masses all arriving at $v_{\text{jet}}$. Error on this calculated mass spectrum, assuming an energy resolution of 15% for the IESA detector and an error on the jet

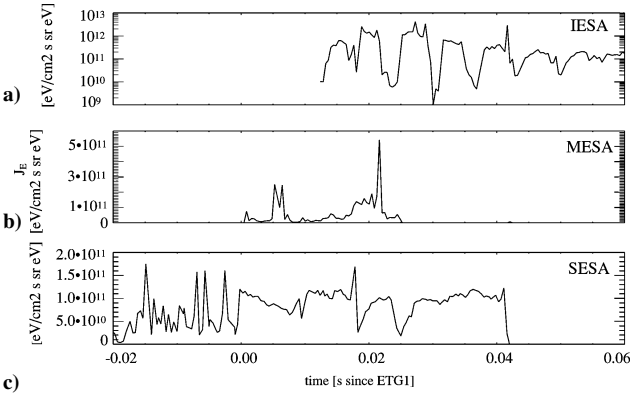


**Fig. 6 Onset of count rate in the IESA, MESA, and SESA as a function of time since $T_{\text{etg1}}$. The prompt response in the electron detectors is a response to UV. Flux error is the same as described for Fig. 3. The diamagetic cavity passage extends from $T_{\text{etg1}} = 0.0175$ to just before $T_{\text{etg1}} = 0.03$ s.**

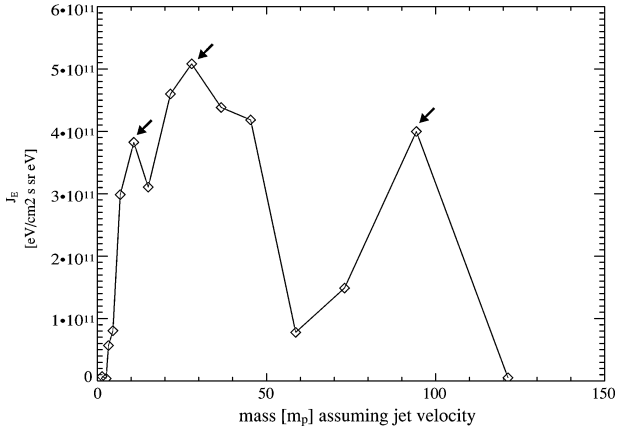


**Fig. 7 Mass spectrum generated by assuming that time-of-flight dispersions in the first sweep of the ion detector come from different masses all arriving at the same initial high velocity. Error in the mass calculation is ±2 amu, as described in the text. Flux error is the same as described for Fig. 3.**

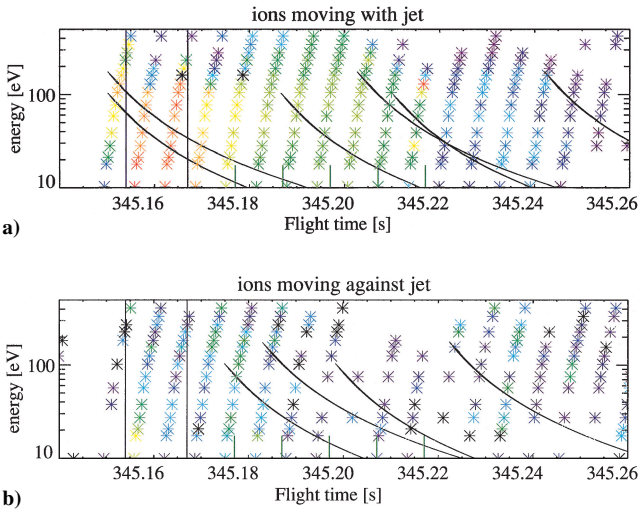


**Fig. 8 Ion energy spectra plotted with the time dispersion of the instrument energy sweep taken into account, for both the toward-jet (panel a) and away-from-jet (panel b) directions. Color qualitatively indicates particle flux, roughly corresponding to the ion color bars of Figs. 3 and 4. The vertical lines indicate the times of the diamagnetic cavity passage. The traces show energy dispersion for aluminum (taller traces) and oxygen (shorter traces) ions moving at the local jet velocity. Successive traces are displaced by two and three gyrotimes; in panel b, the traces are displaced by half a gyrotime.**

velocity of ±3 km/s, is ±2 amu. Structure in this first energy sweep shows peaks consistent with oxgyen [16 atomic mass units (amu)], aluminum (27 amu), and some heavy material (90–100 amu), as indicated by the arrows in Fig. 7. The low-mass, high-speed ions consistent with oxygen arrive just before the diamagnetic cavity, at speeds of 36 km/s.

Another interesting mass-dependent feature of the ion data is the apparent gyrobunching. An examination of Fig. 3 shows the IESA response to be stepped in three bunches: the highest intensity group is coincident with the diamagnetic cavity; the second group runs from $T + 345.17$ to $T + 345.21$; the third from $T + 345.21$ to $T + 345.24$. A qualitative view of this can be seen in Fig. 8, where these same ion spectra are plotted with the time dispersion of the instrument energy sweep taken into account, but now considering both the toward-jet (top) and away-from-jet (bottom) directions. Overlaid on the figure are markers for the diamagnetic cavity passage (vertical lines) and dispersion curves for ions moving at the jet speed at any given time for oxygen (short trace) and aluminum (tall trace). The successive traces are displaced by two and three gyrotimes. In the bottom panel, for the antijet direction, the traces are displaced by half a gyrotime.

The three intensity-level groups seen in Fig. 3 can be seen to be related to the gyrotimes. The first group overlaps with the dispersion curves of the initial passage. The second group overlaps with the dispersion curves displaced by one gyrotime; the third by two gyrotimes. Similarly, in the antijet direction the peak response is displaced from the initial jet response by half a gyrotime. These data are consistent with a picture wherein the ions are created during the initial passage of the jet but then become magnetized after the diamagnetic cavity passes by and begin to gyrate around the PDP.

## Plasma Heating and Plasma Pressure

Next we consider the electron data, showing evidence for wave heating of the ambient electrons and showing plasma pressure in the diamagnetic cavity. Consider first the onset of electron counts shown in Fig. 6. The ion response comes roughly with the approach of the diamagnetic cavity, but both electron detectors appear to respond almost immediately to the explosion, at almost $T_{\text{etg1}} + 0$ s. It appears that this is a response in the detectors to the UV pulse accompanying the explosion.[1] In fact, the SESA response from $T_{\text{etg1}} + 0$ to $T_{\text{etg1}} + 0.007$ s has the same temporal shape as the PDP measurements of UV at 350 nm. The MESA response includes a similar, but lower intensity component, which is swamped by a larger signature matching the UV signal at 310 nm, which peaks at $T_{\text{etg1}} + 0.005$ to $T_{\text{etg1}} + 0.007$ s. The differing responses in the two detectors stem from the fact that the MESA aperture includes the jet direction and is therefore most susceptible to direct UV entry, while the SESA aperture is broadside to the jet, and UV must make several bounces to enter the active region of the SESA.

The true electron response to the first explosion begins at $T_{\text{etg1}} + 0.007$ s in both the SESA and the MESA, where the electron count rate begins to rise in both detectors. Remember that the diamagnetic cavity is not seen until $T_{\text{etg1}} + 0.020$ s, and the ion response begins at $T_{\text{etg1}} + 0.014$ s. The onset of electron counts is coincident with the arrival at the wave electric field detectors of precursor lower hybrid waves at the local ambient oxygen lower hybrid frequency, near 7 kHz. These waves are shown in Fig. 9. Wave data are discussed more fully in Ref. 4. As discussed in the Introduction, rapid ionization from CIV requires a feedback mechanism whereby the ionized jet releases energy in waves that heats electrons and enables further ionization. Given the existence of these lower hybrid waves, we can look to the electron data to see whether there is apparent electron heating. The electron detectors can provide the electron plasma temperature in the leading edge of the diamagnetic cavity (saturated thereafter.) Figure 10 shows the electron distribution function as seen by the two electron detectors, from which the temperature is

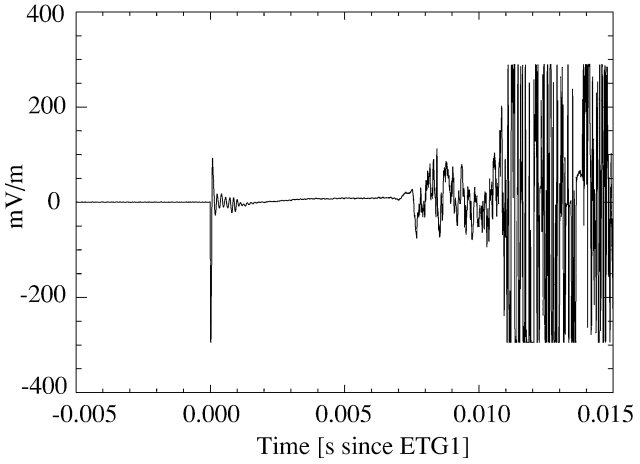


**Fig. 9 Wave electric field data from PDP channel VLF15, as a function of time since the first explosion. Resolution is $\pm 0.6$ $\mu$V/m.**

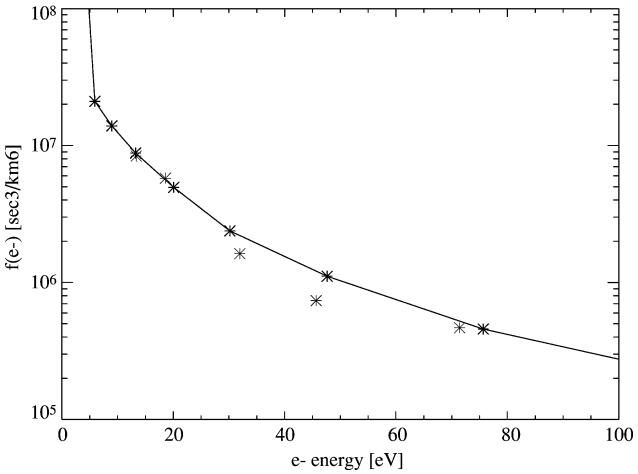


**Fig. 10 Electron distribution function as seen by the two electron detectors, with a temperature of 11–12 eV.**

calculated as

$$T_e = -0.454 \times \frac{\partial \log(f)}{\partial \epsilon} \tag{3}$$

assuming a Maxwellian distribution. The electron temperature thus calculated is approximately 11–12 eV, well above the expected ambient ionospheric temperature of $< 1$ eV.

Given the electron heating and the diamagnetic cavity, it is of interest to see whether the observed plasma pressure is sufficient to create the observed cavity. We can compare the heated electron kinetic pressure, using the Langmuir probe data for $n_e$:

$$n_e k_B T_{e-} = (10^9 \pm 10^4/\text{cc}) \times (k_B) \times (11.5 \pm 1\,\text{eV}) \times (1.16 \times 10^4\,\text{K/eV}) \tag{4}$$

$$= 0.0018 \pm 0.0002\,\text{Pa} \tag{5}$$

to the magnetic pressure outside the cavity:

$$\frac{B^2}{2\mu_0} = \frac{(45 \pm 1\,\mu T)^2}{(8\pi \times 10^{-7})} = 0.0008 \pm 0.00002\,\text{Pa} \tag{6}$$

to see that indeed the observed particle pressure is greater than the ambient magnetic field pressure. The plasma $\beta$ within the diamagnetic cavity is given by

$$\beta = 2\mu_0 n_e k_B T_e \big/ B^2 = 370 \pm 100 \tag{7}$$

using the observed minimum value of $5 \pm 0.5$ $\mu T$ inside the cavity.

## CIV Effects

Several aspects of the particle observations can be viewed in the framework of a CIV interaction with a wave-heating feedback loop, as discussed in the Introduction. It is interesting to consider whether the observed ionization could have been created by these CIV-feedback mechanisms within the short time between the observations and $T_{\text{etg1}}$; also of interest is the temporal duration of the observed ionization. We consider first the creation of the ionization. The electron impact ionization rate from the heated electrons, given an initial CIV seeding to create the ionized jet, is given by

$$\frac{\partial n_i}{\partial t} = n_n \sigma n_e v_e \tag{8}$$

The neutral density is of course decreasing geometrically with distance from the explosion, and the electron flux measurement is available only in the first contact of the jet with the PDP (before the electron detector saturates) and so our measurement will of necessity be

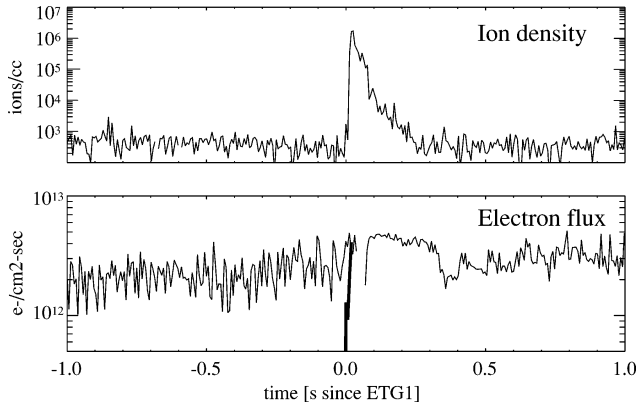


**Fig. 11 Ion density and electron flux used in CIV calculation. Errors given in the text [see Eq. (12) and following discussion].**

only a lower limit on the possible ionization rate. However, for the APEX observations at the PDP we have

$$n_n = (6.6 \pm 0.1) \times 10^{10}/\text{cc} \tag{9}$$

$$\sigma = (4.7 \pm 0.1) \times 10^{-16}\,\text{cm}^2 \tag{10}$$

(from Ref. 15),

$$n_e \times v_e = 4 \times 10^{12} \pm 1 \times 10^8/\text{cm}^2\text{s} \tag{11}$$

so that

$$\frac{\partial n_i}{\partial t} = (1.2 \pm 0.05) \times 10^8/\text{ccs} \tag{12}$$

The ionization reaches the diagnostic payload at $\delta t = 0.013$ s after the explosion. We can thus expect to see, from CIV effects,

$$n_i(\text{CIV}) = \frac{\partial n_i}{\partial t} \times \delta t \tag{13}$$

or

$$n_i(\text{CIV}) = (1.6 \pm 0.2) \times 10^6/\text{cc} \tag{14}$$

This is comparable to the particle detector observations of ions above 10 eV, peaking at $(1.7 \pm 0.1) \times 10^6$/cc. Figure 11 illustrates the electron flux and ion density observations used in this calculation and comparison. Thus the calculated ionization rate is capable of producing the observations in the fast leading edge of the plasma jet. However, this value is considerably less than the Langmuir-probe observations of ion density, which reach $1 \times 10^9$/cc. The particle data and Langmuir-probe data match only in the earliest phase of the burst, when only the fastest ions have reached the payload. The calculated ionization rate does not preclude CIV-feedback generation of this high ionization density because 1) the electron flux measurement becomes saturated and is therefore not a true measure of the peak electron flux and 2) the ionization rate measured at the PDP does not reflect the history of the ionization rate within the traveling jet; the ionization rate might well be considerably higher closer to the explosion, and the observed ionization is cumulative since the creation of the jet. A comparison of APEX and CRIT II (barium) release experiment parameters for this calculation is given in Table 2.

Next we consider the duration of the observed ionization. We have noted that the ion data showed three gyrobunches, each approximately 0.03 s in duration. A study of the Langmuir-probe data in Fig. 2 shows that the peak ionization period, with ion density above 1e8/cc, lasts for 0.015 s, or until $T_{\text{etg1}} + 0.03$ s. What causes the sharp drop in ionization at $T_{\text{etg1}} + 0.03$ s, and again at $T_{\text{etg1}} + 0.05$? It appears to be caused by the jet velocity falling below the critical threshold for seeding the CIV process.

As discussed in the Introduction, the CIV process requires that the relative speed between the neutrals and the plasma be greater than the critical velocity

$$V_{\text{crit}} = \sqrt{2e\Phi/m} \tag{15}$$

**Table 2 Experiment comparison[a]**

| Quantity | CRIT II | Apex |
|---|---|---|
| Distance, m | 1500 | 466 |
| Ion energy flux, keV/cm$^2$ sr s keV | 5e9 | 4e11 |
| $n_i$, /cc (observed) | 1e3 | 1.7e6 |
| $j_e$, /cm$^2$ sr keV | 5e12 | 4e12 |
| $n_n$, /cc | 1e8 (Ba) | 6.6e10 (Al) |
| $\sigma$, $1e{-}16$ cm$^2$ | 12 | 4.7 |
| $\partial n_i/\partial t$, /ccs | 6e5 | 1.2e8 |
| $\delta t$, s | 0.13 | 0.013 |
| $n_i$, /cc (calculated) | 7.8e4 | 1.6e6 |

[a]Comparison between CRIT II and APEX parameters and observations. Errors as described in the text.

**Table 3 CIV parameters[a]**

| Quantity | Al (APEX) | O (APEX) | Ba (CRIT II) |
|---|---|---|---|
| $\Phi_{\text{ionization}}$ | 7.5 | 14 | 5 eV |
| $m_i$ | 27 | 16 | 137 $m_p$ |
| $V_{\text{crit}}$ | 7.3 | 13 | 2.65 m/s |
| $v_{1\,\text{jet}}$ | 36 | 36 | 13 m/s |
| $t^{*b}$ | 0.052 | 0.029 | 0.49 s |
| $\epsilon(v_{1\,\text{jet}})$ | 183 | 108 | 100 eV |
| $\epsilon(V_{\text{crit}}/\sqrt{\eta})$ | 9 | 17 | 6 eV |

[a]Calculation of CIV speeds and times for different species and different experiments. Errors as described in the text.
[b]$t^*$ = time when $v_{\text{jet}} < V_{\text{crit}}/\sqrt{\eta}$.

At relative speeds greater than $V_{\text{crit}}/\sqrt{\eta}$, where $\eta$ is an efficiency factor of not more than 0.67 (Ref. 16), the neutral jet will ionize, creating an unstable plasma jet. For speeds slower than this, the entire CIV-feedback loop process is shut off. As the jet passes the PDP, there is a time-of-flight velocity dispersion effect; the initial observations are of the highest-speed components of the jet, with the slower ones following after. Thus we can look to see at what time does the observed jet fall below the critical velocity. Table 3 lists the various parameters of this calculation, for both aluminum and oxygen CIV effects in the APEX experiment and for barium effects in the CRIT II experiment. We can see that after $T_{\text{etg1}} + 0.029$ s, we are observing at the PDP portions of the jet moving slower than the critical speed for oxygen ionization, and after $T_{\text{etg1}} + 0.052$, slower than the critical speed for aluminum ionization. These are the two times when the ion density drops sharply, first for the high-density, low-energy ions seen by the Langmuir probe but not the particle detectors and second by the low-density, high-energy ions seen in the first gyrobunch in the particle detectors.

Three more points should be noted here. First, the high density of ions seen in the Langmuir probe must consist of particles with energies below the 10 eV threshold of the particle detector, which does not see them. Thus these ions must have been created through the secondary wave-heated feedback loop rather than directly from CIV ionization, because we can see in Table 3 that the lowest-energy direct CIV ion is 9 eV for oxygen and 17 eV for aluminum, both within the observable energy range for the IESA. However, the existence of this high-density, low-energy population is controlled by the direct CIV process, as seen by the shutoff times matching the times at which the jet speed falls below critical.

Second, note the high ionization yield, presumably from CIV, of this particular experiment. The highest ion densities are nearly $(3 \times 10^9 \pm 1 \times 10^4)$/cc at the PDP (see Fig. 2), and the neutral jet density at the PDP is $(6.6 \pm 0.1) \times 10^{10}$/cc, giving a yield of nearly $5(\pm 0.1)\%$. This, like the high yields of the Porcupine[6] and CRIT-II (Ref. 7) experiments, is well above that seen in other similar experiments such as CONDOR.[9]

Finally, during the second event later in the flight a much more muted particle response is seen. Whether the difference between the particle responses in the first and second explosion is caused

by 1) the artificial air cloud released in ETG1 or 2) poor alignment between the jet and the PDP in ETG2 is not known at this time.

## Conclusions

Oxygen (16 amu), aluminum (27 amu), and heavier ions (90–100 amu, presumably debris from the detonation) are seen before, during, and after the passage of the diamagnetic cavity. The fastest ions appear at velocities of 36 km/s, before the diamagnetic cavity. The ions decrease in intensity over 100 ms, stepping down in intensity in three gyrobunches, with the duration of the first gyrobunch apparently controlled by the jet speed falling below the critical velocity for aluminum ionization. The observed electron fluxes (before electron detector saturation) are sufficient to cause enough critical-ionization-velocity (CIV) feedback ionization to account for the observed hot ions but not for the low energy thermal ion population seen by the Langmuir probes. Electric field wave activity at the local oxygen lower hybrid frequency is observed as expected as part of the CIV-wave heating feedback loop and is thought to be the cause of the electron heating and thermal ion ionization.

These observations are consistent with those reported for earlier experiments, but the extensive measurements and good alignment of the Active Plasma Experiment mission (APEX) experiment allows some further clarifications. In particular, in the CRIT II experiment ambient oxygen was also ionized by the CIV process. However, we can see in the APEX experiment that the CIV-affected ambient oxygen, which is pushed ahead of the neutral jet (the "snowplow effect"), apparently controls the dominant source of ionization, which is heated electron impact ionization of thermal oxygen. When the jet speed falls below the critical speed for oxygen CIV ionization, the large yields (5%) fall by over an order of magnitude. When the jet speed falls below the critical speed for aluminum, there is a further reduction in the ion density (seen as the end of the first gyrobunch in the IESA data), but the yields here, although consistent with the observed heated electron flux, are much lower.

Thus we can see in the APEX data set that the ionization lifetime is clearly controlled by the CIV processes, with clear dropoffs both when the jet speed falls to $V_{\text{crit}}(O^+)$ and $V_{\text{crit}}(Al^+)$. Ionization seen after $T_{\text{etg1}} + 0.052$ comes from the gyration of magnetized ions trapped near the payload after the diamagnetic cavity has moved on.

Higher-energy ions seen by the ion electrostatic analyzer are possibly heated by the same lower hybrid wave activity that heats the electron population, and the rich wave data set available for this experiment is worthy of future study.

## Acknowledgments

The APEX project was supported at the University of New Hampshire (UNH) under Applied Physics Laboratory Contract 791103. The UNH instrumentation was designed and engineered by David Rau at UNH. Vehicles and launch facilities were provided by the NASA Wallops Flight Facility Sounding Rocket Office and the University of Alaska Geophysical Institute at Poker Flat.

## References

[1]Erlandson, R. E., Meng, C.-I., Morrison, D., Swaminathan, P. K., Virenda Dogra, V. K., Kumar, C. K., Stoyanov, B. J., Zetzer, J. I., Kiselev, Y., Gavrilov, B. G., Stenbaek-Nielsen, H., Lynch, K. A., Pfaff, R., and Gatsonis, N. A., "The APEX North Star Experiment: Observations of High-Speed Plasma Jets Injected Perpendicular to the Magnetic Field," *Advances in Space Research*, Vol. 29, No. 9, 2002, pp. 1317–1326.

[2]Erlandson, R. E., Meng, C. I., Swaminathan, P. K., Kumar, C. K., Dogra, V. K., Stoyanov, B. J., Gavrilov, B. G., Kiselev, Y., Zetzer, J. I., Stenbaek-Nielsen, H. C., Lynch, K. A., Pfaff, R. F., Delamere, P. A., Bounds, S., and Gatsonis, N. A., "North Star Plasma-Jet Space Experiment," *Journal of Spacecraft and Rockets*, Vol. 41, No. 4, 2004, pp. 483–489.

[3]Gavrilov, B. G., Podgorny, I. M., Sobyanin, D. B., Zetzer, J. I., Erlandson, R. E., Meng, C. I., Pfaff, R. F., and Lynch, K. A., "North Star Plasma-Jet Experiment Particles and Electric and Magnetic Field Measurements," *Journal of Spacecraft and Rockets*, Vol. 41, No. 4, 2004, pp. 490–495.

[4]Pfaff, R. F., Freudenreich, H. T., Bounds, S., Delamere, P. A., Erlandson, R. E., Meng, C. I., Zetzer, J. I., and Gavrilov, B. G., "Electric Field, Magnetic Field, and Density Measurements on the Active Plasma Experiment," *Journal of Spacecraft and Rockets*, Vol. 41, No. 4, 2004, pp. 521–532.

[5]Alfvén, H., *On the Origin of the Solar System*, Oxford Univ. Press, New York, 1954.

[6]Haerendel, G., "Alfvén's Critical Velocity Effect Tested in Space," *Zeitschrift für Naturforschung, A*, Heft 8, Vol. 37, Aug. 1982, pp. 728–735.

[7]Torbert, R. B., "Review of Ionospheric CIV Experiments," *Advances in Space Research*, Vol. 10, No. 7, 1990, pp. 7–16.

[8]Newell, P. T., "Review of the Critical Ionization Velocity Effect in Space," *Review of Geophysics*, Vol. 23, No. 1, 1985, pp. 93–104.

[9]Kelley, M. C., Pfaff, R., and Haerendel, G., "Electric Field Measurements During the CONDOR Critical Velocity Experiment," *Journal of Geophysical Research*, Vol. 91, No. A9, 1986, pp. 9939–9946.

[10]Torbert, R. B., Kletzing, C. A., Liou, K., and Rau, D., "Prompt Ionization in the CRIT-II Barium Releases," *Geophysical Research Letters*, Vol. 19, No. 10, 1992, pp. 973–976.

[11]Stenbaek-Nielsen, H. C., Wescott, E., Haerendel, G., and Valenzuela, A., "Optical Observations on the CRIT-II Critical Ionization Velocity Experiment," *Geophysical Research Letters*, Vol. 17, No. 10, 1990, pp. 1601–1604.

[12]Swenson, C. M., Kelley, M. C., Primdahl, F., and Baker, K. D., "CRIT II Electric, Magnetic, and Density Measurements Within an Ionizing Neutral Stream," *Geophysical Research Letters*, Vol. 17, No. 12, 1990, pp. 2337–2340.

[13]Wescott, E., Stenbaek-Nielsen, H., and Torbert, R., "CRIT-II: Observations and Consequences of Non-Illuminated Emissions at 4554a and 6300a from the Neutral Barium Jets," *EOS Transactions of the American Geophysical Union*, Vol. 70, Oct. 1989, p. 1278.

[14]Carlson, C. W., Curtis, D. W., Paschmann, G., and Michael, W., "An Instrument for Rapidly Measuring Plasma Distribution Functions with High Resolution," *Advances in Space Research*, Vol. 2, No. 7, 1983, pp. 67–70.

[15]Kiefer, L. J., and Dunn, G. H., "Ionization Cross Section Data," *Reviews of Modern Physics*, Vol. 38, No. 1, 1966, pp. 1–35.

[16]Formisano, V., Galeev, A. A., and Sagdeev, R. Z., "The Role of the Critical Ionization Velocity Phenomena in the Production of Inner Coma Cometary Plasma," *Planetary and Space Science*, Vol. 30, No. 5, 1982, pp. 491–497.

D. L. Cooke
*Guest Editor*

**Color reproductions courtesy of Dartmouth College.**